

# Collective plasma effects of electron-positron pairs in beam-driven QED cascades

Kenan Qu,<sup>1</sup> Sebastian Meuren,<sup>1,2</sup> and Nathaniel J. Fisch<sup>1</sup>

<sup>1</sup>*Department of Astrophysical Sciences, Princeton University, Princeton, New Jersey 08544, USA*

<sup>2</sup>*Stanford PULSE Institute, SLAC National Accelerator Laboratory, Menlo Park, California 94025, USA*

(Dated: 26 October 2021)

Understanding the interplay of strong-field QED and collective plasma effects is important for explaining extreme astrophysical environments like magnetars. It has been shown that QED pair plasmas is possible to be produced and observed by passing a relativistic electron beam through an intense laser field. This paper presents in detail multiple sets of 3D QED-PIC simulations to show the creation of pair plasmas in the QED cascade. The beam driven method enables a high pair particle density and also a low particle gamma factor, which both play equal rolls on exhibiting large collective plasma effects. Finite laser frequency upshift is observed with both ideal parameters (24 PW laser laser colliding with 300 GeV electron beam) and with existing technologies (3 PW laser laser colliding with 30 GeV electron beam).

## I. INTRODUCTION

The *QED plasma regime* is an emerging topic which studies the interplay between the strong-field quantum and collective plasma effects when the Schwinger field is greatly exceeded. This regime dictates the dynamics of intriguing astrophysical environments like magnetars<sup>1,2</sup>, binary neutron-star mergers<sup>3,4</sup>, and core-collapse supernovae explosions<sup>5,6</sup>. Understanding the plasma physics of these extreme environments<sup>7-9</sup>, including for the emerging field of multi-messenger astronomy<sup>10-14</sup>, is critical. For example, magnetars<sup>15-19</sup> are filled with strong-field QED cascades of relativistic electron-positron pair plasma<sup>20-23</sup> in their magnetospheres. The relativistic particle emission in the varying magnetic field of magnetars is very likely responsible for the Fast Radio Bursts<sup>24-27</sup>.

Tremendous effects have been made to understand the QED plasma dynamics<sup>28-47</sup> and to explore possibilities of their preparation in laboratories<sup>48-60</sup>. The QED plasma dynamics<sup>9,60-62</sup> is characterized by strong field QED and collective plasma effects. The QED nonlinearity is observed only in fields above the QED critical limit  $10^{18} \text{ Vm}^{-1}$ , often called Schwinger limit<sup>63</sup>. In such a strong field, high energy photons and electron-positron pairs are created in a cascaded manner<sup>64-75</sup>. The required particle density to manifest collective plasma effect depends on the observation method. Emission in the infrared wavelength (to which the detectors are most sensitive) corresponds to a particle density of near  $10^{25} \sim 10^{27} \text{ m}^{-3}$ . For a  $1 \mu\text{m}^{-3}$  volume, the total charge of pair plasma needs to reach  $0.001 \text{ nC} \sim 0.1 \text{ nC}$ .

In a recent publication<sup>60</sup>, we demonstrated the generation of a quasi-neutral pair-plasma with a density that is comparable to the critical one by using the combination of a 30 PW laser and a dense 300 GeV electron beam or by using less stringent parameters. This method circumvents the technological limitations by taking advantage of the high quality energetic electron beam facilities to boost the laser intensity in the particle rest frame.

## A. $e^-$ -beam-driven cascade v.s. all-optical method

We need to work in the rest frame of high energy particle beams, because reaching the Schwinger field limit directly in laboratories is still beyond the extend of current technology. A multi-GeV electron beam from a particle accelerator have a gamma factor of over  $10^4$ , which can boost the laser fields by the same number. The seminal SLAC E-144 experiment<sup>76,77</sup> has already used this method to observe evidences of nonlinear Compton scattering and Breit-Wheeler pair production by colliding a  $\sim 10^{18} \text{ Wcm}^{-2}$  laser and a  $\sim 50 \text{ GeV}$  electron beam. Due to relatively low laser intensity, only a limited number of positrons were produced to exhibit any collective plasma effects. The upcoming experiment SLAC FACET-II will deploy a new laser with over  $10^{20} \text{ Wcm}^{-2}$  peak intensity. Combined with the LCLS-Cu LINAC<sup>78-80</sup>, pair multiplication factor over unity can be achieved providing a unique opportunity to explore nonperturbative QED cascade.

The counterpart of beam-driven QED cascade is by using two colliding ultra-strong lasers. The strong beat accelerates the seed electrons to the relativistic speed, which in turn boosts the laser field amplitude. As soon as the QED critical field is reached in the electron rest frame, high energy photons are emitted and pairs are created. The strong laser continues to accelerate the particles to induce a QED cascade. With sufficiently strong laser field, QED cascade is manifested in the rest frame of the pair particles and the created pair plasmas. It was proposed<sup>48</sup> that laser intensities above  $10^{24} \text{ Wcm}^{-2}$  is sufficient to probe the QED critical field in the particle rest frame. This all-optical method has prompted investigation both analytically and numerically<sup>48-59</sup>. However, the  $10^{24} \text{ Wcm}^{-2}$  laser intensity required by the all-optical method needs a highly non-trivial tight focus of a 100 PW laser<sup>81-83</sup>. Solving this challenge will depend on substantial development beyond current state-of-the-art laser technology. Even if the pair plasma is created, the pair particles have a large gamma factor of  $\sim 10^3$  which

greatly suppresses the plasma frequency observed in the laboratory frame.

Compared with the all-optical method, the beam-driven approach lowers the laser intensity requirement by two orders of magnitudes. This is owing to that the particle accelerators can produce multi-GeV or even tens of GeV electron beam energy, corresponding to gamma factors of  $10^4 \sim 10^5$ . A PW-level laser can already induce QED pair multiplication. Such laser systems are routinely operated in several laboratories<sup>84</sup>. The all-optical method only accelerates the electrons to a gamma factor similar to the laser dimensionless amplitude  $a$ ; Even reaching  $\gamma \sim 10^3$  needs laser intensity of over  $10^{24} \text{ Wcm}^{-2}$ <sup>48-59</sup> and thus requires large 100 PW-scale laser facilities<sup>81-83</sup>.

## B. Producibility v.s. observability of the pair plasmas

As the pair density grows in a QED cascade, they begin to behave collectively as a plasma. Existing experimental detectors like magnetic spectrometer can only distinguish electron and positron particles but cannot measure the pair density or test collective plasma effect. The figure of merit for collective plasma dynamics is determined by the plasma frequency ( $\omega_p$ ) which is proportional to the ratio of pair particle density ( $n_p$ ) and pair gamma factor ( $\gamma$ ), *i.e.*,  $\omega_p \propto n_p/\gamma$ . The inverse proportionality to the pair gamma factor favors the beam-driven approach over the all-optical approach. Since the average pair gamma factor is similar to the laser dimensionless amplitude, the lower laser intensity needed for the beam-driven approach greatly reduces the average gamma factor of the produced pair plasma. It thus exhibits higher plasma frequency even if the colliding lasers can produce the same plasma density. The counter propagating laser pulse and pairs also provide possibilities to further slow down the pairs through laser radiation pressure. Thus, the pair plasma created in a beam-driven QED cascade is easier to detect than one created with the all-optical approach.

The laser which is used to create the pair plasma also informs the pair plasma frequency through its change of spectrum. Both as the pair plasma forms and as it slows down, the plasma frequency increases inside the laser field. The increase of plasma frequency abruptly reduces the vacuum refractive index which the laser is mediated. The consequence is that the laser frequency is upshifted and laser wavelength is blue shifted, according to the theory of temporal change of optical refractive index<sup>85-94</sup>. The pair oscillation, which is responsible for the laser frequency upshift, is coupled to the intense laser field to radiate a strong signal. Thus, remarkably, despite the small plasma volume and despite the relativistic plasma motion, signatures of the QED plasma regime might be identified experimentally with state-of-the-art technology. On the contrary, the small plasma volume ( $\mu\text{m}$ -scale) eliminates

the possibility of using conventional detection methods, *e.g.*, by observing plasma instabilities like the two-stream instability<sup>95</sup>, the Weibel instability<sup>96</sup>, or stimulated Brillouin scattering (SBS)<sup>97</sup>.

This paper is organized in the following structure: In Sec. II, we briefly review the process of QED cascade in an electron-beam-laser collision. This offers the background for explaining our numerical simulation results. In Sec. III, we introduce the setup of our 3D PIC QED simulations and show the production of electron-positron pairs. In Sec. IV, we focus on the pair deceleration through both synchrotron emission and through laser radiation pressure. The important pair reflection condition is introduced here. In Sec. V, we analyze the laser dynamics and show how its spectrum changes with the increasing plasma frequency. Multiple optical detection methods are explained including laser central frequency shift, chirping, and homodyne detection of the laser phases. In Sec. VI, we verify the scaling of the laser frequency shift with different electron beam and laser parameters. In Sec. VII, we demonstrate the possibility of creating and observe a QED plasma using state-of-the-art parameters, *i.e.*, a 3 PW laser and a 30 GeV electron beam. In Sec. VIII, we present our conclusions.

## II. PAIR GENERATION THROUGH BEAM-DRIVEN QED CASCADE

We first provide a brief overview of the QED cascade process. In an electron-beam-driven QED cascade, an energetic electron beam collides with a counter-propagating strong laser field. The laser amplitude is greatly boosted to exceed the critical field  $E_s$  in the electron rest frame. Thus, the electrons emit photons which further split into electron-positron pairs. Each of the pair particles, given sufficient energy, can continue the photon emission and pair generation process to induce a cascaded generation of pairs. The process converts high electron beam energy into large pair numbers. In this section, we layout the properties of beam-driven QED cascade while we briefly explain how the electron-positron pairs are generated.

In the initial stage of the collision, the electron beam has the maximum energy with a Lorentz factor  $\gamma$ . It boosts the counter-propagating laser field by the same factor  $\gamma$  in the rest frame of the electrons. Such a boost aims to produce a large quantum parameter  $\chi_e = E^*/E_s = \gamma|\mathbf{E}_\perp + \beta \times c\mathbf{B}|/E_s$ , where  $\mathbf{E}$  and  $\mathbf{B}$  are the electric and magnetic field of the laser in the laboratory frame, and  $\beta$  is the electron beam speed normalized to the speed of light  $c$ . The strong laser field drives the electron motion, causing emission of photons<sup>64,98</sup>.

The photon emission spectra differ depending on the quantum parameter  $\chi_e$ . The regime  $\chi_e \gtrsim 1$  is reached near the laser intensity peaks where quantum synchrotron emission causes the electrons to emit almost

all of its energy into a single gamma ray. In the regions of low laser intensity  $\chi_e \ll 1$ , the emission is classical. The emitted photon  $\hbar\omega$  only takes a small portion of the electron energy  $\mathcal{E}$ , *i.e.*,  $\hbar\omega \sim \chi_e \mathcal{E}$ . These low energy photons would escape the laser focus spot without decaying into pairs.

The high-energy gamma ray photons are highly likely to decay into an electron-positron pair in the same strong laser field. For the interest of this paper, we focus on the Breit-Wheeler process that a photon decays into one pair of electron and positron. The decaying process also depends on the quantum parameter of the emitted photon  $\chi_\gamma = [\hbar\omega/(2m_e c^2)] |\mathbf{E}_\perp + \mathbf{k} \times c\mathbf{B}|/E_s$  with  $\hbar\omega(\hbar\mathbf{k})$  being the photon energy (momentum), and  $m_e$  being the electron rest mass. The pair generation happens only when  $\chi_\gamma$  is above the unit threshold value. For  $\chi_\gamma \gg 1$ , the photon transfers almost all of its energy to either the electron or positron, while for smaller  $\chi_\gamma$  values the photon energy is more symmetrically partitioned.

Therefore, a very intense laser can cause a cascade of gamma rays and pairs from a single energetic electron. Each subsequent emission and decay process transfers the energy into predominantly to one new particle and creates many other particles with lower energies. The gamma photon decay process first terminates when  $\chi_\gamma < 1$  though the high-energy pairs continue to emit photons until  $\chi_e \ll 1$ . For an electron beam with original gamma factor  $\gamma_0$  and density  $n_e$  and a laser with dimensionless amplitude  $a_0 \equiv eE/(m_e c^2 \omega_0)$  and frequency  $\omega_0$ , the pair multiplication rate is approximately

$$n_p \sim \tilde{\chi} n_e, \quad \tilde{\chi} \approx 2a_0 \gamma_0 (\hbar\omega_0)/(m_e c^2). \quad (1)$$

This relation holds only if the laser pulse is sufficiently wide and long. The multiplication rate for finite laser pulse waist and duration could cause deviation from the estimation of multiplication, but the linear scaling should nevertheless hold in general.

The plasma frequency  $\omega_p = \sqrt{e^2 n_p / (\gamma m_e \epsilon_0)}$  is dependent on the ratio of particle density  $n_p$  and mass  $\gamma m_e$ . Hence, the collective effects, if they were to be probed, are manifested through the oscillation of the low energy particles in the strong laser field. Since the pair formation rate  $t_f \sim (2a_0 \omega_0)^{-1}$  is inversely proportional to the laser amplitude  $a_0 (\gg 1)$ , the pairs are more likely to be created when the laser is strong, which thereby drives the strongest collective pair oscillation.

### III. 3D PIC QED SIMULATIONS OF PAIR CREATION

To set up the electron-beam and laser collision for QED cascade, the above analysis shows that it requires including an intense laser field with  $a_0 \gg 1$  and an electron beam with high  $\gamma$  factor such that  $\chi_e \gtrsim 1$ . Towards this limit, we consider head-on collision of a 1 nC electron beam of 300 GeV<sup>99,100</sup>, shown as a blue sphere in Fig. 1, and a 24 PW laser pulse<sup>82</sup> with wavelength  $\lambda = 0.8 \mu\text{m}$ , shown as a yellow spheroid. The corresponding

dimensionless laser amplitude is  $a_0 \approx 170$  and the quantum parameter is  $\tilde{\chi}_e \approx 220$  at the Gaussian waist in the focal plane, and  $\tilde{\chi}_e \approx 600$  at the laser focus.

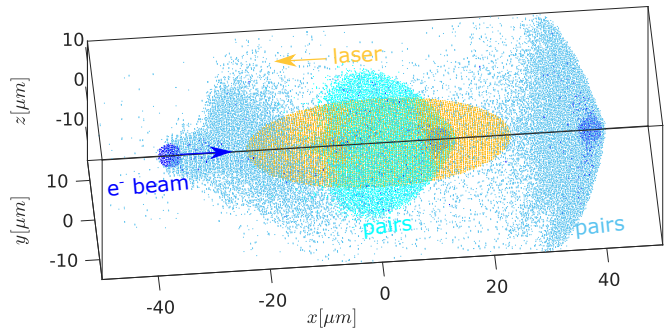


FIG. 1. Schematics of the 3D QED-PIC simulation of a beam-driven cascade. An energetic electron beam (deep blue) collides with a multi-PW laser pulse (yellow) and creates an electron-positron pair plasma by inducing a QED cascade. The volume of the pair plasma at different times is denoted as green ( $t = 0.21\text{ps}$ ) and light blue ( $t = 0.3\text{ps}$ ) dots.

The electron beam has a spherical Gaussian number density  $n_e(\mathbf{r}) = n_{e0} \exp[-r^2/(2r_0^2)]$ , where  $n_{e0} = 4 \times 10^{20} \text{ cm}^{-3}$  is the peak density and  $r_0 = 1 \mu\text{m}$  is the rms radius of the sphere. The counter-propagating laser pulse is linearly polarized in the  $y$  direction and propagates in the  $-x$  direction. It has a Gaussian distribution in both transverse and longitudinal directions with  $I = I_0 \cdot [w_0/w(x)]^2 \exp[-2\rho^2/w^2(x)] \exp[-2t^2/\tau^2]$  where  $I_0 = 6 \times 10^{22} \text{ Wcm}^{-2}$  is the peak intensity,  $w_0 = 5 \mu\text{m}$  is the waist at  $x = 0$ ,  $w(x) = w_0 \sqrt{1 + (x/x_R)^2}$ ,  $x_R = \pi w_0^2/\lambda \approx 98 \mu\text{m}$  is the Rayleigh length, and  $\tau = 50 \text{ fs}$  is the pulse duration (intensity FWHM:  $\sqrt{2 \log(2)}\tau \approx 59 \text{ fs}$ , electrical field FWHM:  $2\sqrt{\log(2)}\tau \approx 83 \text{ fs}$ ). Each dot in Fig. 1(a) represents a region with pair density above  $2 \times 10^{20} \text{ cm}^{-3}$  or laser intensity above  $5 \times 10^{20} \text{ Wcm}^{-2}$ .

The simulations were performed using the PIC code EPOCH<sup>101,102</sup> with the QED module<sup>53,59,73</sup>. The simulation box measured  $100 \mu\text{m} \times 30 \mu\text{m} \times 30 \mu\text{m}$  is discretized into  $4000 \times 300 \times 300$  cells. The charged particles are represented by near  $6 \times 10^8$  computing particles. The time step is determined by the Courant–Friedrichs–Lewy condition and the inverse plasma frequency, *i.e.*, it is chosen as the smaller value of the minimum plasma oscillation period in any cells and the smallest cell dimension multiplied by  $0.95/c$ . The actual time step in our simulations is  $0.083 \text{ fs}$ , which is well below the maximum possible photon emission time<sup>102</sup>  $t_f \gtrsim 0.36 \text{ fs}$  in all our simulations.

With the large quantum parameter  $\tilde{\chi}_e$ , the collision quickly creates a pair plasma with an increasing charge number. Figure 2(a) shows the evolution of total charge of the injected electrons (blue) and created electrons (red). The injected electron remains 1 nC throughout the interaction. Pair electrons charge first grows exponentially until it reaches the 139 nC total charge at  $\sim 0.2 \text{ ps}$  and remains unchanged afterwards.

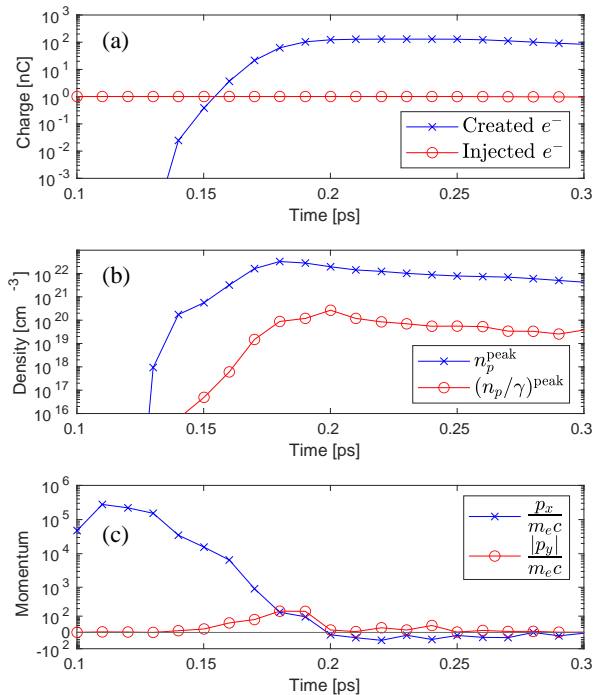


FIG. 2. (a) Evolution of total charges of the injected electrons (blue) and created electrons (red). (b) Evolution of the peak pair plasma density  $n_p$  (blue), and the parameter  $n_p/\gamma$  (red) which determines the laser frequency upshift. (c) Evolution of the pair particle momenta in the longitudinal (blue) and transverse (red) directions, normalized to  $m_e c$ . The local particle density  $n_p$ , gamma factor  $\gamma$ , and momentum  $p_{x,y}$  are taken their respective averaged value in a single simulation cell.

The peak density of the created pairs, shown as the blue curve in Fig. 2(b), quickly grows to a peak value of  $n_p = 82n_{e0} = 3.28 \times 10^{22} \text{ cm}^{-3}$ , but begins to slowly decrease at 0.17 ps. The decrease of peak density is caused by plasma volume expansion, illustrated at three different stages in Fig. 1a. Since the pair particles are mostly created in the region of strong laser field, the pair particles immediately accelerate transversely causing volume expansion. The transverse motion also allows the particle to escape the high intensity laser focus resulting in a lower total charge than predicted by Eq. (1).

To get more insight of the dynamics of pair generation, we analyze the pair density and momentum at the center line  $y = z = 0$  with peak laser intensity, shown in Fig. 3 and Fig. 4. The top row of these two figures show the snapshot at 0.16 ps. At this time, the center of the electron sphere has not reached the laser focal plane though a significant amount of pairs have been generated. The density plot in Fig. 3(a) shows that the generated pairs are limited to the region near the electron beam. The gamma factor plot in Fig. 3(b) shows that the electron beam energy is decreased by 2 ~ 3

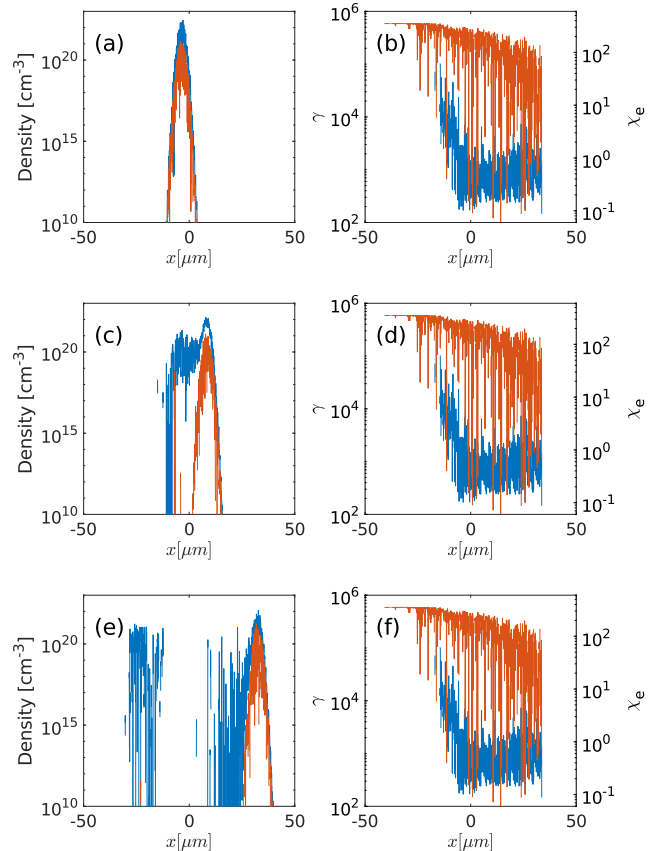


FIG. 3. The density (left column) and gamma factor  $\gamma$  (right column) of the injected electrons (blue) and created electrons (red) at line  $y = z = 0$ . The electron quantum factor  $\chi_e$  is calculated at the peak laser amplitude  $a_0 = 170$ . The three rows show the snapshots at 0.16 ps (a-b), 0.2 ps (c-d), and 0.28 ps (e-f), respectively.

orders of magnitude from its initial value  $\gamma_0 = 6 \times 10^5$  after passing through the laser peak. The generated pairs have an energy of near  $10^3 m_e c^2$ , corresponding a quantum parameter of  $\chi_e \lesssim 1$ , after passing through the laser peak. This is the lowest particle energy that can be efficiently generated via the photon decay process. Beyond this point, the gamma photons can no longer decay into pairs and the QED cascade terminates, which can be seen from the saturation of charge growth in Fig. 2(a). However, the pairs continue to lose energy, which we will explain in detail in the following section.

#### IV. PAIR DECELERATION AND PAIR REFLECTION

We observed and explained in the previous section that the injected electron beam would emit high energy photons which decay into pair particles in a strong laser field until the photon energy (and hence the generated pair energy) decreases to  $\chi_\gamma \lesssim 1$  when the QED cascade

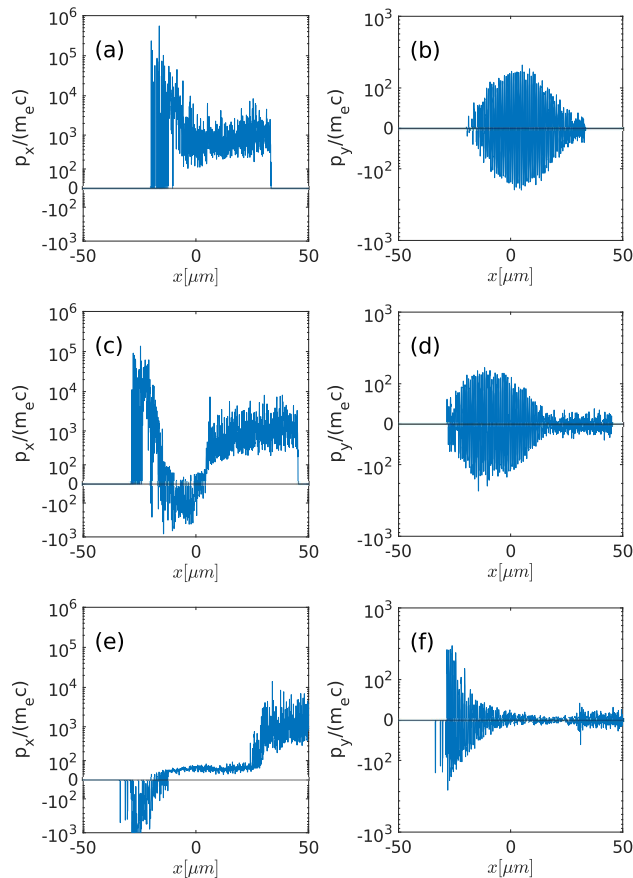


FIG. 4. The longitudinal  $p_x$  (left column) and transverse  $p_y$  (right column) momenta of the injected electrons (blue) and created electrons (red) at line  $y = z = 0$ , normalized  $m_e c$ . The three rows show the snapshots at 0.16 ps (a-b), 0.2 ps (c-d), and 0.28 ps (e-f), respectively.

terminates. The pairs, however, continue to lose energy via synchrotron radiation, as shown in Fig. 2(c).

The photon emission is dominated by quantum synchrotron radiation when  $\chi_e \gtrsim 0.1$ . The decrease of pair energy can be seen in Fig. 3(d) and (f), which shows the snapshot immediately after the center of the electron sphere passes through the laser peak. The blue curve in Fig. 3(d) shows that the generated pair energy further decreases to  $10^2 m_e c^2$ , corresponding to  $\chi_e \sim 0.1$ , at the tail of the electron beam. Depending on the laser amplitude  $a_0$ , quantum synchrotron emission can reduce the pair gamma factor to

$$\gamma \lesssim 0.1 \frac{\gamma_0}{\chi_e} \approx \frac{0.05 m_e c^2}{a_0 \hbar \omega_0}. \quad (2)$$

Figure 3(c) shows that these low-energy pairs are created through the secondary generation from the daughter pairs, and thereby they tailgate the injected electron beam.

Quantum synchrotron emission stops when  $\chi_e$  reaches  $\sim 0.1$ , and classical radiation emission begins to

dominate<sup>64</sup>. The pair particles wiggle in the laser field to radiate electromagnetically with negligible quantum contributions like recoil or spin. The strong laser field drives transverse motion of the pairs, evidenced in Fig 4(b,d) for that the transverse pair momentum  $p_y$  is enveloped by the laser profile and that  $|p_y|/(m_e c) = a_0$  locally. Due to the conservation of canonical momentum, each charged particle transfer the amount of  $a_0^2 m_e c / (4\gamma)$  longitudinal momentum to a counter-propagating laser field upon entering it. It means that particles can be stopped or even reflected by the strong laser field if they have sufficiently low longitudinal momentum, *i.e.*,  $p_x \lesssim a_0^2 m_e c / (4\gamma)$ , or equivalently,  $\gamma \sim a_0^{103}$ . By comparing this condition with Eq. (2), we find that particle reflection is possible if

$$a_{0,\text{th}} \gtrsim \sqrt{0.05 m_e c^2 / (\hbar \omega_0)}, \quad (3)$$

for a sufficiently long laser pulse. For optical lasers with  $\hbar \omega_0 \sim 1$  eV, the threshold is approximately  $a_{0,\text{th}} \gtrsim 100$ , corresponding to intensity  $I_{\text{th}} \gtrsim 10^{22}-10^{23} \text{ W cm}^{-2}$ . Particle reflection is shown in Fig. 2(c) and Fig. 4(c) and (e) as the pair longitudinal momentum  $p_x$  becomes negative near the laser peak. The reflected pair can also be observed in Fig. 1(c) as the spreading pairs (light blue dots) throughout the simulation box at  $t = 0.2$  ps.

The particle reflection threshold is very important in probing the collective pair effects because the pair particle mass reaches their minimum value as they stop longitudinally. Since plasma dynamics is manifested through plasma frequency  $\omega_p$  which is proportional to  $\sqrt{n_p/\gamma}$ , achieving lower particle energy is equally important with higher particle density. Thus, we plot the parameter  $n_p/\gamma$  in Fig. 2(b). The red curve shows that the parameter  $n_p/\gamma$  continues to increase even after the pair density reaches its peak value  $n_p = 3.28 \times 10^{22} \text{ cm}^{-3}$  at  $t = 0.18$  ps. The pair momentum  $p_x$  and  $p_y$  decreases to its minimum value at  $t = 0.2$  ps when  $n_p/\gamma$  reaches its peak value of  $2.67 \times 10^{20} \text{ cm}^{-3}$  at  $t = 0.2$  ps. Thus, the beneficial synchrotron radiation, which keeps reducing the pair energy, outweighs the density increase between  $t = 0.18$  ps and  $t = 0.2$  ps until finally the latter effect dominates.

While the strong laser field causes the pairs to lose longitudinal momentum  $p_x$ , it at the same time increases the transverse momentum  $p_y$ . The maximum value of  $p_y$  is identical to local laser amplitude  $a_0$  due to conservation of canonical momentum. Therefore, the minimum pair gamma factor is equal to the laser amplitude  $\gamma = a_0$  provided that the particle reflection threshold condition Eq. (3) is satisfied. This is evident in Fig. 3(d) and (f) which shows a minimum gamma factor of  $\gamma \lesssim 100$ . Note that the particle reflection may happen behind the laser peak if we consider the finite time of particle deceleration by synchrotron radiation.

Thus, we provide the following ‘‘rule of thumb’’ for the maximum achievable pair plasma density and the

relevant gamma factor

$$n_p \sim \tilde{\chi}_e n_e, \quad \gamma_f \sim a_0. \quad (4)$$

These relations are valid if the laser is above the threshold intensity  $I_{th}$  for particle reflection [Eq. (3)], and if the interaction time is long enough such that the cascade reaches its asymptotic state.

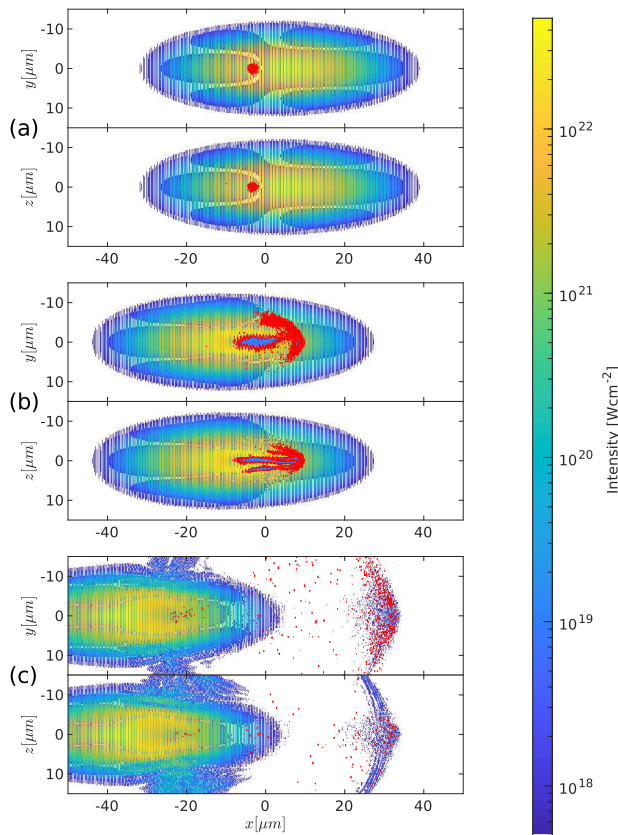


FIG. 5. The two panels of each subplot show the laser profiles at the  $z = 0$  cross section and  $y = 0$  cross section, respectively. The red dots show the regions of  $n_p/\gamma > 1 \times 10^{19} \text{ cm}^{-3}$  at the corresponding planes. The snapshots are taken at 0.16 ps (a), 0.2 ps (b), and 0.28 ps (c), respectively

To illustrate the creation of pairs more clearly, we plot the profiles of pair density and laser intensity in the  $y = 0$  plane and  $z = 0$  plane as the top and bottom panels of Fig. 5, respectively. Each red dot denotes a region with  $n_p/\gamma > 1 \times 10^{19} \text{ cm}^{-3}$  at the corresponding plane. It is seen in Fig. 5(a) that the pairs are initially created nearby the injected electron beam. The pairs then expands to mainly the transverse directions shortly after the creation. Linear laser polarization breaks the cylindrical symmetry of pair motion. The  $y$ -polarized laser naturally accelerates the pairs more strongly in the  $y$  direction than in the  $z$  direction, which is seen in Fig. 5(b). The asymmetry of pair expansion increases as

shown in Fig. 5(c). Figure 5(c) also reveals rich dynamics of the laser profile, which will be discussed in detail in the following section.

## V. LASER BEAM DIFFRACTION AND FREQUENCY UPCONVERSION

Since the pair generation rate is proportional to the laser amplitude, the pairs are dominantly created near the peak laser field. The strong laser field thus drives pairs into oscillation immediately after they are generated. Transverse current is induced from the pair oscillation which radiates electromagnetic fields. With non-negligible pair density, the radiation could reach a detectable level to reveal the pair dynamics. When the pair density reaches near the critical density, the radiation becomes strongly coupled to the input laser, causing a quantitative upshift of the laser frequency. Measuring the change of laser frequency allows us to unambiguously probe the collective pair plasma effects.

For a given input laser, the amount of laser blue shift reveals the plasma frequency of the pairs. Macroscopically, laser frequency upshift arises from non-adiabatic change of index of refraction, which determines the phase velocity of light. Suddenly created pairs reduces the index of refraction thereby increasing the laser phase velocity. It corresponds to increased local laser wave oscillation in the region of pairs and hence upshift of laser frequency.

Microscopically, the laser frequency upshift can be analyzed through finding the transverse current  $\mathbf{J}_\perp$  of the pair particles. As the pairs are almost always generated when strong laser field is present, they are immediately driven into an oscillatory motion. Assuming the pair particles have no transverse momentum at the time of generation. The laser field with vector potential  $\mathbf{A}$  can transfer transverse momentum of  $\mathbf{p}_\perp = e\mathbf{A}_\perp$  to the pairs. Thus, the pair transverse current is  $\mathbf{J}_\perp = 2en_p\mathbf{p}_\perp/(\gamma m_e) = (2e^2n_p/m_e)\mathbf{A}_\perp/\gamma = \epsilon_0\omega_p^2\mathbf{A}_\perp$ . Here, we define the plasma frequency  $\omega_p = [2n_p e^2/(\gamma m_e \epsilon_0)]^{1/2}$ . The factor of two accounts for the equal contribution of positrons and electrons to the laser dispersion relation. The transverse current couples to the laser field through the wave equation

$$\nabla^2 \mathbf{A}_\perp - \frac{1}{c^2} \partial_t^2 \mathbf{A}_\perp = -\frac{e^2}{m_e c^2 \epsilon_0} \frac{2n_p}{\gamma} \mathbf{A}_\perp \equiv -\frac{\omega_p^2}{c^2} \mathbf{A}_\perp, \quad (5)$$

from which we see that a non-adiabatic change of plasma frequency  $\omega_p^2 \propto n_p/\gamma$  induces a change of laser frequency  $\omega$ . If the plasma frequency is small compared with the input laser frequency  $\omega_p \ll \omega$ , the laser frequency is approximated as

$$\omega \cong \omega_0 + \omega_p^2/(2\omega_0). \quad (6)$$

If the plasma is created non-instantly, the change of laser frequency needs to take an integral over the plasma

frequency change at the retarded position  $X = x + c(t - t')$ :

$$\omega(x, t) = \omega_0(x) + \frac{1}{2\omega_0} \int_0^t dt' [\partial_T \omega_p^2(X, T)]_{X=x+c(t-t')}^{T=t'} \quad (7)$$

The laser wave vector changes correspondingly obeying the dispersion relation

$$\begin{aligned} k(x, t) &\cong \omega(x, t)/c - \omega_p^2(x, t)/(2\omega_0 c) \\ &= k_0(x) + \frac{1}{2\omega_0} \int_0^t dt' [\partial_X \omega_p^2(X, T)]_{X=x+c(t-t')}^{T=t'} \quad (8) \end{aligned}$$

Equations (7) and (8) demonstrate that the change of laser frequency and wave vector is determined by the total temporal and spatial change of plasma density, respectively. In the limit of instantaneous plasma creation, the upshift of frequency and wave vector after interaction reduce to a simple form  $\Delta\omega \equiv \omega - \omega_0 = \omega_p^2/(2\omega_0)$  and  $\Delta k \equiv k - k_0 = \omega_p^2/(2c^2 k_0)$ . The relation of the instantaneous laser frequency and wave vector becomes very useful for interpreting our numerical simulation results: whereas experiments measure the laser frequency at a specific location, numerical simulations often more conveniently output the laser wave vector at a specific time. Equations. (7) and (8) provides a definite relation to transform the laser wave vector upshift into frequency upshift during the QED cascade.

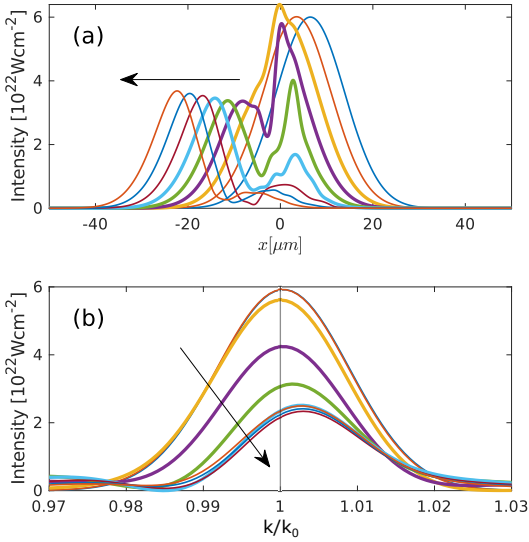


FIG. 6. (a) The laser pulse intensity envelopes between  $t = 0.16$  ps and  $0.24$  ps in the direction of the arrow. (b) The laser intensity spectra at the corresponding times.

For the simulation under consideration, the peak value of  $n_p/\gamma$  corresponds to 6.7% of the critical plasma density at rest  $n_c \approx 1.71 \times 10^{21} \text{ cm}^{-3}$  of the drive laser. Accordingly, a laser frequency upshift is observed in the intensity spectra displayed in Fig. 6. Figure 6(a) shows the laser intensity in its propagation axis  $y = z = 0$  with

each curve corresponding to from  $t = 0.16$  ps to  $0.24$  ps, respectively, in the direction of the arrow. Figure 6(b) shows the corresponding intensity spectra by Fourier transformation. The peaks of the spectra before and after the collision reveals a wave vector upshift  $\Delta k/k_0 = 0.2\%$ . Since the pair plasma counter propagates with the laser pulse, the laser wave vector spectrum becomes equivalent to the frequency spectrum after the collision: 0.2% is also the laser frequency upshift. This finite frequency upshift is caused by the small fraction of laser overlap with the electron beam. Specifically, the frequency-upconverted photons are confined to a small region, whereas the majority of laser photons are not upconverted.

The oscillation motion of the high density pairs absorbs a significant amount of laser energy. It causes a decrease of laser peak intensity, which can be observed in Fig. 6. We highlight this process between  $t = 0.18$  ps and  $0.21$  ps as thick curves in Fig. 6(a). This period corresponds to when the pair parameter  $n_p/\gamma$  approaches its peak value, as can be seen from Fig. 2(b). Actually, the pairs, after absorbing the laser energy, radiate to the whole space. It is reflected in Fig. 6(a) as splitting of the laser peak when the pairs are generated and laser frequency is upshifted. While the main laser peak continues to propagate to the  $-x$  direction, a second peak is developed at  $t = 0.19$  ps (thick purple curve) and propagates towards the  $+x$  direction.

Due to the small volume of the pairs, they emit a point-source-like radiation, as shown in Fig. 6(c). The large radiation angle can actually be used advantageous for experimental detection: It can be captured by an optical detector installed separated from the path of laser beam. The radiation is near the laser frequency and is hence easily distinguished from the high energy gamma photons.

Much higher laser frequency upshift can be obtained when focusing on the region where pairs are quickly created. Such a laser spectrogram is typically obtained in experiments using techniques like frequency-resolved optical gating<sup>104</sup> or spectral shear interferometry for direct electric field reconstruction<sup>105</sup>. Numerically, we conduct a wavelet transform of the laser pulse and obtain precisely the laser photon wave vectors at different pulse positions plotted as red curves in Fig. 7. We also plot the pair particle density in the  $z = 0$  plane to demonstrate the correlation of pair plasma creation and laser wave vector upshift. Figure 7(a) shows that the wave vector spectrum becomes chirped immediately at the region of plasma creation near  $x = 0$ . The wave vector chirps up in the front of the interaction region and chirps down in the tail, which agrees with Eq. (8). As the pair density increases and the interaction continues, the amplitude of chirp grows, as seen in Fig. 7(b). The chirped region propagates along the laser direction [Fig. 7(c)] and gets separated with the pair plasma. Thus, it can eventually be collected by a detector and reveals as a chirped frequency spectrum. The maximum photon frequency shift reaches  $\Delta\omega/\omega_0 = 2.4\%$ .

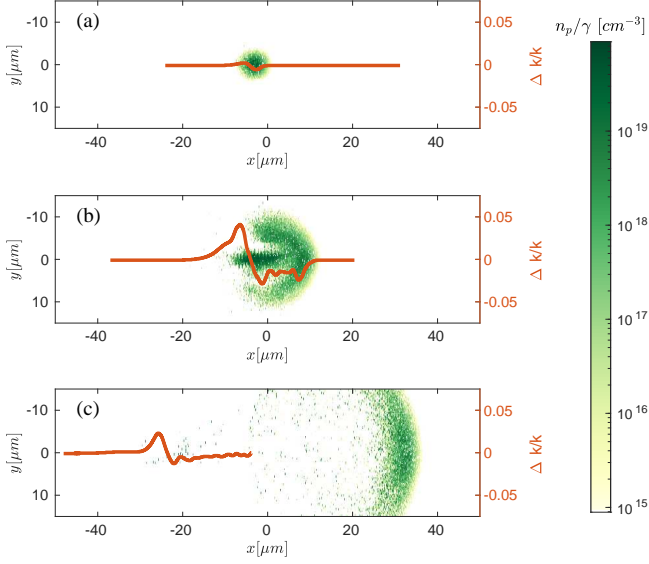


FIG. 7. The pair parameter  $n_p/\gamma$  and the relative laser wave number change  $\Delta k/k$ . The snapshots are taken at 0.16 ps (a), 0.2 ps (b), and 0.28 ps (c), respectively.

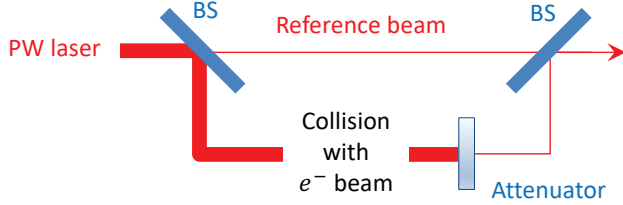


FIG. 8. Interferometer setup for homodyne detection of the change in laser profile. A weak reference beam is split from the strong PW laser using a beam splitter (BS) with a large reflection ratio. The same reference beam is then combined with the attenuated post-interaction PW laser to produce the interference signal.

The small disturbance in laser phase and intensity can be precisely measured with an interferometer. As shown in Fig. 8, the strong laser is first sent through a beam splitter with a large reflection ratio. A small fraction of the laser pulse is split to serve as a reference beam, whose electric field can be denoted as  $E_r = E_{r0}(\mathbf{r}, t)e^{-i\omega_0 t} + c.c.$ . The strong laser pulse, after interacting with the electron beam, becomes  $E = E_0(\mathbf{r}, t)e^{-i\omega_0 t + i\varphi} + c.c.$ . Here,  $\varphi \equiv \int_0^t \Delta\omega dt'$  represents the accumulated local phase change and  $E_0(\mathbf{r}, t)$  denotes the new envelope. The pulse is then attenuated to the same amplitude with the reference beam before they are combined through another beam splitter. The interference signal, called a homodyne signal, is

$$\Delta I = \frac{1}{T} \int_0^T \frac{c\varepsilon_0}{2} |E_r - E|^2 dt, \quad (9)$$

where the negative sign arises from the double reflection

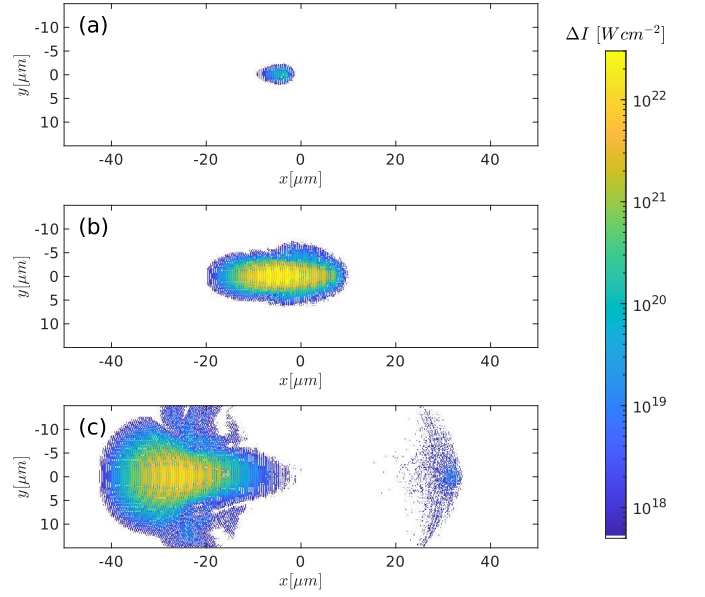


FIG. 9. The homodyne signal which shows the change of laser beam intensity profile at the  $z = 0$  cross section. The snapshots are taken at 0.16 ps (a), 0.2 ps (b), and 0.28 ps (c), respectively.

of the PW laser and the signal is averaged through an optical cycle  $T = 2\pi/\omega_0$  to model the slow response time of the photo detector. The homodyne signal is sensitive to both the laser phase fluctuation and change of envelope. For only a small phase fluctuation  $\varphi \ll 2\pi$ , the homodyne signal is

$$\Delta I \propto [1 - \cos(\varphi)]I_{r0} \approx \varphi I_{r0}, \quad (10)$$

where  $I_{r0}$  is the intensity of the reference beam. Since  $\varphi = \int_0^t \Delta\omega dt'$ , one can find out the frequency shift  $\Delta\omega$  through  $\Delta I/I_{r0}$ . Note that the proportional relation in Eq. (10) only holds for  $\Delta I \ll I_{r0}$ .

Numerically, we show the homodyne signal  $(c\varepsilon_0/2)|E_r - E|^2$  at three different snapshot in Fig. 9. The reference beam is obtain via a separate simulation of the same laser beam without encountering the electron beam. The interference signifies the change of electromagnetic field. It confirms that the radiation starts at the location where pairs are generated and then expands to the whole space. The radiation pattern in Fig. 9(c) consists of two types of signals, including a pattern that propagates a long the laser direction and a pattern that radiates to the whole space. The propagation radiation pattern is the result of interference of phase-shifted post-interaction beam and the reference beam. The latter radiation pattern is the point-source-like pair emission.

Our simulation assumes linearly polarized laser with an electric field in the  $y$ -direction. Compared to a circularly polarized laser, the linear polarization can achieve  $\sqrt{2}$ -fold higher peak field amplitude at the same laser energy. Although the circularly polarized laser has



a constant amplitude, the exponential dependence of the pair growth rate obviously favors higher amplitude of linear polarization.

## VI. SCALING OF THE LASER FREQUENCY UPSHIFT

Since upconversion of laser frequency is determined by the pair plasma frequency, it provides an unambiguous signature of collective plasma effects in beam-driven QED cascades. In the previous section, our 3D PIC simulations demonstrate the collective pair plasma effects during pair creation and energy decay, and show how the plasma signature is imprinted in the colliding laser. For the best results of illustration, the collision uses a 24 PW laser pulse and a 1 nC electron beam at 300 GeV. But can existing technology produce sufficiently high density pair plasma to exhibit observable collective effects? In this section, we answer the question by finding how the amount of frequency upshift scales with different parameters of the laser and electron beam.

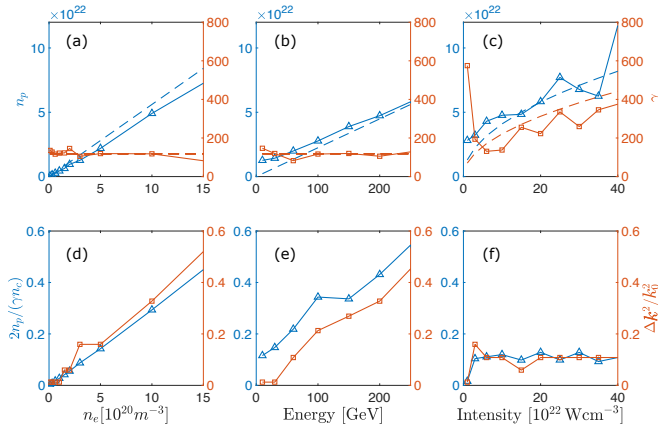


FIG. 10. The top row shows the dependence of the peak density  $n_p$  and Lorentz factor  $\gamma$  of the created pairs. The bottom row shows prediction and actual peak values of the relative frequency upshift of the laser pulses. The marked curves show the results obtained through 1D PIC simulations with the following parameters unless shown otherwise: electron beam peak density  $n_p = 4 \times 10^{19} \text{ m}^{-3}$ , rms duration  $1 \mu\text{m}/c$ , energy 100 GeV; and laser peak intensity  $3 \times 10^{22} \text{ Wcm}^{-2}$ , and duration 100 fs.

It is made clear in Eqs. (5) and (6) that the magnitude of pair plasma radiation is determined by the pair plasma parameter  $n_p/\gamma$ , *i.e.*, plasma density divided by pair energy. The spatial profile of the radiation depends on the pair size at the time of pair creation. High pair density is achieved through high input electron beam density  $n_e$  and large pair multiplication rate  $\tilde{\chi}$ , which, according to Eq. (1), is proportional to the laser amplitude  $a_0$ , laser frequency  $\omega_0$ , and electron beam energy  $\gamma_0 m_e c^2$ .

For exhibiting collective effects, an equally important parameter is the pair energy or gamma factor. In a QED

cascade, the pair energy decreases as a result of radiation recoil and ponderomotive potential of the laser field, as we explained in Sec. IV. The minimum pair energy is reached when the laser intensity meets the threshold for pair reflection, as shown in Eq. (3). Then, the pair motion becomes purely transverse and the pair gamma factor is  $a_0$ , as shown in Eq. (4). By combining Eq. (6) with Eq. (4), we find

$$\omega_f^2/\omega_0^2 - 1 \sim \frac{\tilde{\chi}_e n_e}{n_c a_0} \sim \gamma_0 \frac{\hbar \omega_0}{m_e c^2} \frac{n_e}{n_c} \quad (11)$$

for the frequency upshift. This relation holds if the laser pulse is sufficiently long and intense such that the QED cascade fully develops and the pair plasma is eventually stopped and reflected.

To verify Eq. (11), we conduct a series of 1D QED-PIC simulations with different electron beam densities, beam energies, and laser intensities. The 1D simulations discretize  $150 \mu\text{m}$ -long box into 48000 cells. Both the envelopes of the electron beam density and the laser intensity have the same Gaussian shape as in the 3D simulations at  $y = z = 0$ . The laser pulse parameters are  $I_0 = 3 \times 10^{22} \text{ Wcm}^{-2}$  (corresponding to  $a_0 = 120$  and  $\tilde{\chi}_e = 40$ ),  $w_0 = 2.5 \mu\text{m}$ , and  $\tau = 50$  fs. The 1D simulations neglect transverse effects such as plasma inhomogeneity and laser diffraction, but keep three dimensional particle momenta and currents, which are critical for inducing the laser frequency upshift.

The results are shown in Fig. 10. The panels (a-b) consider electron beams with varying peak densities and energies colliding with a laser pulse with peak amplitude  $a_0 = 120$  ( $3 \times 10^{22} \text{ Wcm}^{-2}$ ), respectively. As  $\tilde{\chi}_e \propto \gamma_0$ , either increasing beam density or beam energy causes a linear increase of the created pair plasma density, whereas the final gamma factor remains constant at about  $a_0$ . The results are in agreement with Eq. (4). The maximum frequency upshift shown in Fig. 10(d), and 10(e) obtained from the wavelet transform also shows decent agreement with Eq. (11).

Figures 10(c) and 10(f) scan the laser intensity  $I$  from  $10^{22} \text{ Wcm}^{-2}$  ( $a_0 = 70$ ) to  $4 \times 10^{23} \text{ Wcm}^{-2}$  ( $a_0 = 430$ ). For fixed electron beam energy the quantum parameter changes as  $\tilde{\chi}_e \propto \sqrt{I}$ . Therefore, we expect the final plasma density  $n_p$  to show a similar scaling. Figure 10(f) clearly demonstrates the threshold dependence of the frequency upshift on the laser intensity. When the laser intensity is below  $3 \times 10^{22} \text{ Wcm}^{-2}$ , the pair reflection condition [Eq. (3)] is not satisfied and the cascade does not saturate within the pulse duration, causing minimum laser frequency upshift. But above the threshold amplitude, the quantity  $n_p/\gamma$  becomes independent of the laser intensity and the laser frequency upshift reaches its maximum value.

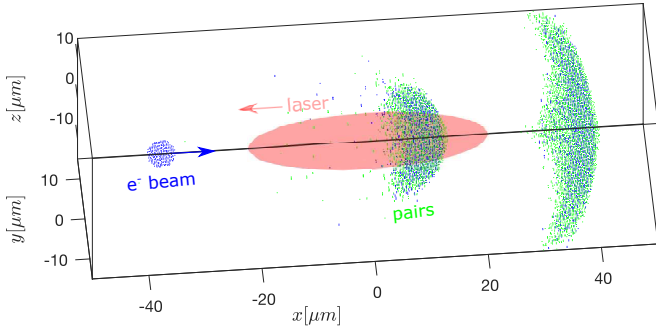


FIG. 11. 3D simulation of a 30 GeV (blue) electron beam colliding with a 3 PW laser pulse (red). A QED cascade creates a pair plasma (green) with an expanding volume. The electron beam itself also expands due to the laser ponderomotive force.

## VII. COLLISION OF 3 PW LASER AND 30 GeV ELECTRON BEAM

In the previous sections, we presented a clear numerical demonstration that the interplay between collective plasma and strong-field quantum effects leaves a characteristic imprint on the driving laser pulse. The upshift of the instantaneous laser frequency, according to the “rule of thumb” [Eq. (11)], becomes experimentally observable by combining a multi-GeV class electron beam with density above  $\sim 10^{20} \text{ cm}^{-3}$  and a laser at  $\sim 10^{22} \text{ Wcm}^{-2}$  intensity. In principle, such beam-driven QED cascades could be initiated with electron beams obtained from either a linear accelerator or laser wakefield acceleration (LWFA) at all-optical laser facilities. But linear accelerators benefit from its much higher total charge number at nC-level compared with pC-level obtained from reported LWFA accelerated electrons<sup>106</sup>. The required electron beam density and beam energy can be obtained with only a moderate upgrade of existing facilities, e.g., SLAC’s FACET-II<sup>107</sup>.

We conduct such 3D QED-PIC simulations to show the prospect. Figure 11 illustrates the simulation of a 50 fs-duration, 2.5  $\mu\text{m}$ -waist, 3 PW ( $3 \times 10^{22} \text{ Wcm}^{-2}$ ) laser pulse colliding with a 1 nC, 30 GeV,  $4 \times 10^{20} \text{ cm}^{-3}$  electron beam. Other numerical parameters are identical to the last 3D simulations. The generated pair plasma and the radiation are shown in Figs. 12 and 13. Figure 12(a) and (b) show that the created electron-positron pair plasma reaches a total charge number of 26 nC and peak density of  $6.8 \times 10^{21} \text{ cm}^{-3}$ . The red dots in Fig. 13 show that the tightly focused laser punches a hole in the pair plasma and pushes the pairs away from the propagation axis. The created pairs begin to escape the simulation box from  $t = 0.23 \text{ ps}$  causing a decrease of total charge number as seen in Fig. 12(a).

With a lower energy, the injected electron beam has a much lower relativistic mass. The electrons are thus expelled by the strong laser ponderomotive force and expand with the created pair plasma. This is seen in

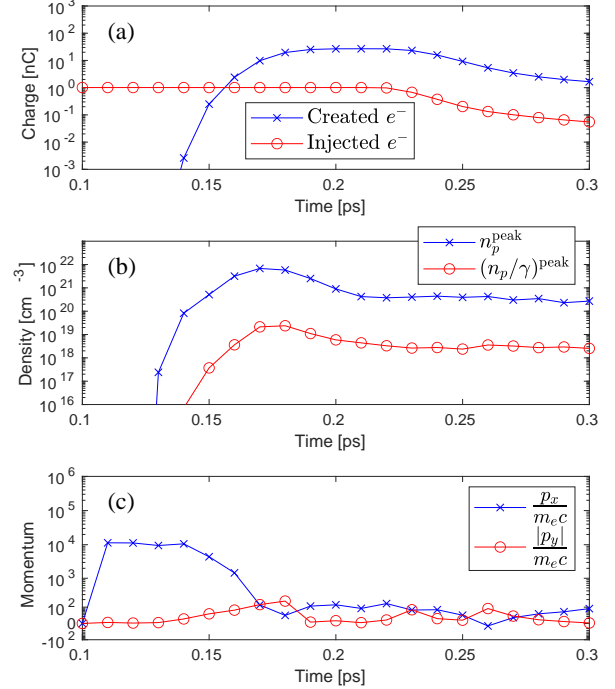


FIG. 12. (a) Evolution of total charges of the injected electrons at 30 GeV (blue) and created electrons (red). (b) Evolution of the peak pair plasma density  $n_p$  (blue), and the parameter  $n_p/\gamma$  (red) which determines the laser frequency upshift. (c) Evolution of the pair particle momenta in the longitudinal (blue) and transverse (red) directions, normalized to  $m_e c$ . The local particle density  $n_p$ , gamma factor  $\gamma$ , and momentum  $p_{x,y}$  are taken their respective averaged value in a single simulation cell.

Fig. 11 shows in which the blue dots mostly overlap with the green shades whereas the blue dots remain a sphere shape in Fig. 1. The expanding electron beam begin to leave the simulation window, causing a decreasing total charge from  $t = 0.23 \text{ ps}$  as seen in Fig. 12(a).

Since the laser intensity meets the threshold value  $a_{0,\text{th}}$  for particle reflection, some pairs reverse their propagation direction. This is confirmed in Fig. 12(c) as the pair longitudinal momentum is about to change sign. The parameter  $n_p/\gamma$  reaches  $2.4 \times 10^{19} \text{ cm}^{-3}$ , corresponding to 1.4% of the critical density of a  $0.8 \mu\text{m}$  laser.

We obtain the instantaneous wave vectors through a wavelet transform of the laser electric field at  $y = z = 0$  and plot them as red curves in Fig. 14. For comparison, we also plot the wave vectors of the same laser without encountering an electron beam as black curves. Due to the tight focus, the laser has a short Rayleigh length and the Gouy phase induces a down chirp of the wave vectors near the focal point. The red curves clearly show a laser wave vector upshift in the region of pair plasma

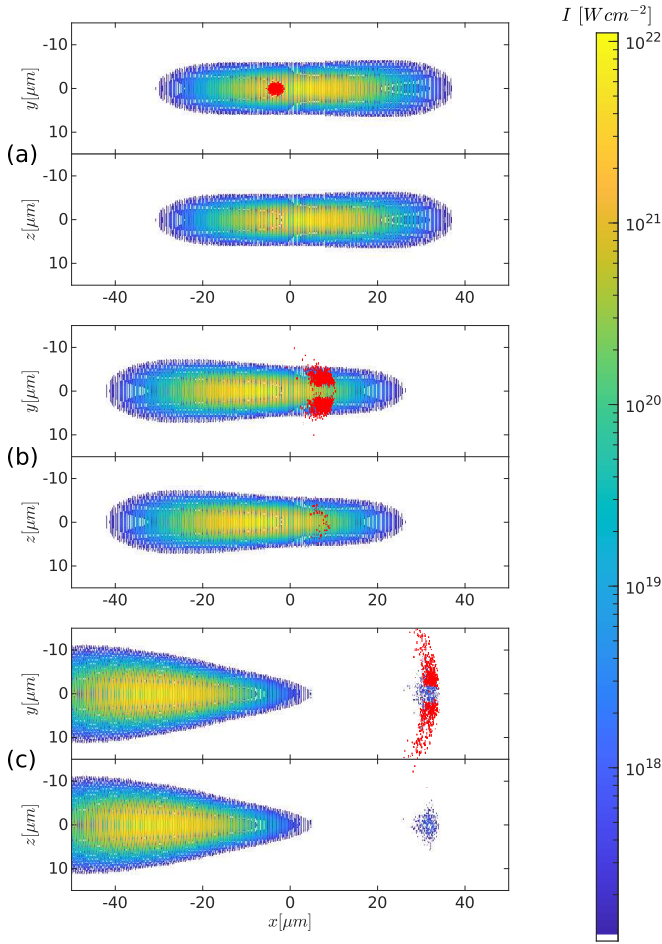


FIG. 13. The two panels of each subplot show the laser profiles at the  $z = 0$  cross section and  $y = 0$  cross section, respectively. The red dots show the regions of  $n_p/\gamma > 1 \times 10^{19} \text{ cm}^{-3}$  at the corresponding planes. The bottom panel shows the change of laser beam intensity profile at the  $z = 0$  cross section. The snapshots are taken at 0.16 ps (a), 0.18 ps (b), and 0.24 ps (c), respectively.

creation. The maximum wave vector upshift reaches a value of  $\sim 0.2\%$ .

In the top panels of Fig. 14, we plot the homodyne signal  $(c\varepsilon_0/2)|E - E_r|$ . Strong signals exhibit in the regions of pair plasma creation. The plots show that the interference signal immediately appears when the pairs are initially created. As the pair density grows, the signal reaches a maximum intensity of  $1.2 \times 10^{20} \text{ Wcm}^{-2}$ , which can be easily detected in an experiment. At 0.18 ps, the homodyne signal intensity increases by  $5 \times 10^{19} \text{ Wcm}^{-2}$  within a single laser period indicating a 0.16% laser wave vector upshift.

## VIII. CONCLUSION AND DISCUSSION

In conclusion, we present QED PIC simulations for creating observable high-density electron-positron

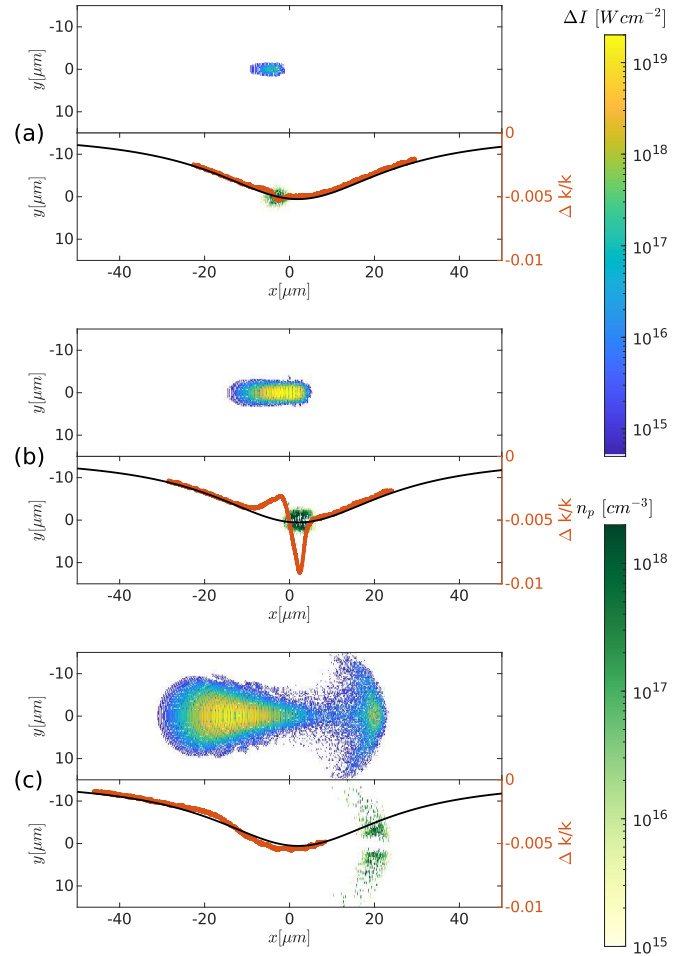


FIG. 14. The top panel of each subplot shows the homodyne signal at the  $z = 0$  cross section. The bottom panel shows the pair parameter  $n_p/\gamma$  at the  $z = 0$  cross section. The red and black curves show the instantaneous wave vectors of the laser field at  $y = z = 0$  with and without encountering the electron beam, respectively. The snapshots are taken at 0.16 ps (a), 0.18 ps (b), and 0.24 ps (c), respectively.

pair plasmas through strong-field QED cascades using existing laser and electron beam technologies. Analysis and numerical simulation demonstrate that both high pair density  $n_p$  and low pair gamma factor  $\gamma$  are equally important for exhibiting strong collective plasma effects. A large pair plasma frequency can be achieved with dense and high-energy electron beam. A higher laser intensity can effectively increase the pair plasma frequency only below the threshold amplitude  $a_{0,\text{th}} \gtrsim 100$  ( $I_{0,\text{th}} \gtrsim 10^{22} \text{ Wcm}^{-2}$ ). Laser intensities above the threshold re-accelerate the pairs in the counter-propagating direction, causing a higher pair gamma factor and thus a lower plasma frequency.

We specifically considered two sets of 3D PIC simulations, including one set with ideal parameters and the other set with existing technologies. The ideal parameter set uses a 24 PW  $\lambda = 0.8 \mu\text{m}$  laser with a waist of  $5 \mu\text{m}$ , duration of 50 fs, and peak intensity of

$6 \times 10^{22} \text{ Wcm}^{-2}$  (corresponding to  $a_0 \approx 170$ ). Combined with a 300 GeV, 1 nC,  $4 \times 10^{20} \text{ cm}^{-3}$  peak density electron beam, it creates a 139 nC plasma with peak density of  $3.28 \times 10^{22} \text{ cm}^{-3}$ , which is 82 times higher than the injected electron beam. The pair parameter  $n_p/\gamma$  reaches a peak value of  $2.67 \times 10^{20} \text{ cm}^{-3}$ , which is 6.7% of the critical density of the laser. The simulation shows a laser frequency upshift of 2.4% at the output and a maximum wave vector upshift of 4.8% during the collision.

We further demonstrate that the collective QED plasma signature can be observed with state-of-the-art technologies. Even a 30 GeV electron beam and a 3PW 2.5  $\mu\text{m}$ -waist laser (other parameters are identity to the previous 3D PIC simulation) can create a pair plasma of  $n_p/\gamma = 2.67 \times 10^{20} \text{ cm}^{-3}$  and induce a 0.2% laser frequency upshift. It suggests how hitherto unobserved collective effects can be probed with existing state-of-the-art laser and beam technologies, suggesting a strong argument for colocating these technologies.

Our results demonstrate that the co-location<sup>108,109</sup> of a dense, 30 GeV electron beam with a 3 – 10PW optical laser enables us to reach the QED plasma regime at substantially lower laser intensities ( $10^{22} \text{ Wcm}^{-2}$ ). Whereas it has been well known that QED cascades can be studied in electron-beam laser collisions<sup>65</sup>, our results recognize the importance of the electron beam density, showing that the beam-compression techniques developed in the context of FACET-II are indeed sufficient to probe the interplay between collective plasma and strong-field quantum effects with a laser-electron-beam setup. In fact, compared to all-optical methods of reaching the QED regime, the use of lower laser intensities reduces the particle mass shift, thereby remarkably makes the QED collective effects easier to observe.

The beam-laser collision setup, together with the proposed observable, opens seminal possibilities for studying laboratory astrophysics and High Energy Density Physics (HEDP) by providing access to the QED plasma regime with available technology.

## ACKNOWLEDGMENTS

This work was supported by NNSA Grant No. DE-NA0002948, and AFOSR Grant No. FA9550-15-1-0391.

- <sup>1</sup>V. M. Kaspi and A. M. Beloborodov, “Magnetars,” *Annu. Rev. Astron. Astrophys.* **55**, 261 (2017).
- <sup>2</sup>B. Cerutti and A. M. Beloborodov, “Electrodynamics of Pulsar Magnetospheres,” *Space Sci. Rev.* **207**, 111 (2017).
- <sup>3</sup>Y. Q. Xue, X. C. Zheng, Y. Li, *et al.*, “A magnetar-powered X-ray transient as the aftermath of a binary neutron-star merger,” *Nature* **568**, 198 (2019).
- <sup>4</sup>D. J. Price and S. Rosswog, “Producing Ultrastrong Magnetic Fields in Neutron Star Mergers,” *Science* **312**, 719 (2006).
- <sup>5</sup>P. Mösta, C. D. Ott, D. Radice, L. F. Roberts, E. Schnetter, and R. Haas, “A large-scale dynamo and magnetoturbulence in rapidly rotating core-collapse supernovae,” *Nature* **528**, 376 (2015).

- <sup>6</sup>S. Akiyama, J. C. Wheeler, D. L. Meier, and I. Lichtenstadt, “The Magnetorotational Instability in Core-Collapse Supernova Explosions,” *Astrophys. J* **584**, 954 (2003).
- <sup>7</sup>D. A. Uzdensky and S. Rightley, “Plasma physics of extreme astrophysical environments,” *Rep. Prog. Phys* **77**, 036902 (2014).
- <sup>8</sup>D. Uzdensky, M. Begelman, A. Beloborodov, *et al.*, “Extreme Plasma Astrophysics,” (2019), [arXiv:1903.05328](https://arxiv.org/abs/1903.05328).
- <sup>9</sup>P. Zhang, S. S. Bulanov, D. Seipt, A. V. Arefiev, and A. G. R. Thomas, “Relativistic plasma physics in supercritical fields,” *Phys. Plasmas* **27**, 050601 (2020).
- <sup>10</sup>M.-H. Wang, S.-K. Ai, Z.-X. Li, N. Xing, H. Gao, and B. Zhang, “Testing the Hypothesis of a Compact-binary-coalescence Origin of Fast Radio Bursts Using a Multimessenger Approach,” *Astrophys. J* **891**, L39 (2020).
- <sup>11</sup>B. P. Abbott, R. Abbott, T. D. Abbott, *et al.*, “GW190425: Observation of a Compact Binary Coalescence with Total Mass  $\sim 3.4M_{\odot}$ ,” *Astrophys. J* **892**, L3 (2020).
- <sup>12</sup>LIGO Scientific Collaboration and Virgo Collaboration, “GW170817: Observation of Gravitational Waves from a Binary Neutron Star Inspiral,” *Phys. Rev. Lett.* **119**, 161101 (2017).
- <sup>13</sup>C. Palenzuela, L. Lehner, M. Ponce, S. L. Liebling, M. Anderson, D. Neilsen, and P. Motl, “Electromagnetic and Gravitational Outputs from Binary-Neutron-Star Coalescence,” *Phys. Rev. Lett.* **111**, 061105 (2013).
- <sup>14</sup>M. Anderson, E. W. Hirschmann, L. Lehner, S. L. Liebling, P. M. Motl, D. Neilsen, C. Palenzuela, and J. E. Tohline, “Magnetized Neutron-Star Mergers and Gravitational-Wave Signals,” *Phys. Rev. Lett.* **100**, 191101 (2008).
- <sup>15</sup>L. Lin, C. F. Zhang, P. Wang, *et al.*, “No pulsed radio emission during a bursting phase of a Galactic magnetar,” *Nature* **587**, 63 (2020).
- <sup>16</sup>A. Ridnaia, D. Svinin, D. Frederiks, A. Bykov, S. Popov, R. Aptekar, S. Golenetskii, A. Lyzenko, A. Tsvetkova, M. Ulanov, and T. L. Cline, “A peculiar hard x-ray counterpart of a galactic fast radio burst,” *Nature Astronomy* **5**, 372 (2021).
- <sup>17</sup>C. K. Li, L. Lin, S. L. Xiong, *et al.*, “HXMT identification of a non-thermal X-ray burst from SGR J1935+2154 and with FRB 200428,” *Nature Astronomy* **5**, 378 (2021).
- <sup>18</sup>C. D. Bochenek, V. Ravi, K. V. Belov, G. Hallinan, J. Kocz, S. R. Kulkarni, and D. L. McKenna, “A fast radio burst associated with a Galactic magnetar,” *Nature* **587**, 59 (2020).
- <sup>19</sup>B. C. Andersen, K. M. Bandura, M. Bhardwaj, *et al.*, “A bright millisecond-duration radio burst from a Galactic magnetar,” *Nature* **587**, 54 (2020).
- <sup>20</sup>A. Y. Chen, F. Cruz, and A. Spitkovsky, “Filling the Magnetospheres of Weak Pulsars,” *Astrophys. J* **889**, 69 (2020).
- <sup>21</sup>A. N. Timokhin and A. K. Harding, “On the Maximum Pair Multiplicity of Pulsar Cascades,” *Astrophys. J* **871**, 12 (2019).
- <sup>22</sup>R. Gueroult, Y. Shi, J.-M. Rax, and N. J. Fisch, “Determining the rotation direction in pulsars,” *Nat. Commun.* **10**, 1 (2019).
- <sup>23</sup>D. B. Melrose and R. Yuen, “Pulsar electrodynamics: an unsolved problem,” *J. Plasma Phys.* **82**, 635820202 (2016).
- <sup>24</sup>B. Marcote, K. Nimmo, J. W. T. Hessels, *et al.*, “A repeating fast radio burst source localized to a nearby spiral galaxy,” *Nature* **577**, 190 (2020).
- <sup>25</sup>The CHIME/FRB Collaboration, “A second source of repeating fast radio bursts,” *Nature* **566**, 235 (2019).
- <sup>26</sup>V. Ravi, M. Catha, L. D’Addario, S. G. Djorgovski, G. Hallinan, R. Hobbs, J. Kocz, S. R. Kulkarni, J. Shi, H. K. Vedantham, S. Weinreb, and D. P. Woody, “A fast radio burst localized to a massive galaxy,” *Nature* **572**, 352 (2019).
- <sup>27</sup>K. W. Bannister, A. T. Deller, C. Phillips, *et al.*, “A single fast radio burst localized to a massive galaxy at cosmological distance,” *Science* **365**, 565 (2019).
- <sup>28</sup>Óscar Amaro and M. Vranic, “Optimal laser focusing for positron production in laser-electron scattering,” (2021), [arXiv:2106.01877 \[physics.plasm-ph\]](https://arxiv.org/abs/2106.01877).
- <sup>29</sup>W. Luo, W.-Y. Liu, T. Yuan, M. Chen, J.-Y. Yu, F.-Y. Li, D. Del Sorbo, C. P. Ridgers, and Z.-M. Sheng, “QED cascade

- saturation in extreme high fields,” *Scientific Reports* **8**, 8400 (2018).
- <sup>30</sup>J.-x. Liu, Y. Zhao, X.-p. Wang, J.-z. Quan, T.-p. Yu, G.-B. Zhang, X.-h. Yang, Y.-y. Ma, F.-q. Shao, and J. Zhao, “High-flux positrons generation via two counter-propagating laser pulses irradiating near-critical-density plasmas,” *Physics of Plasmas* **25**, 103106 (2018).
- <sup>31</sup>Z. Guo, L. Ji, Q. Yu, B. Feng, X. Geng, L. Zhang, W. Wang, and B. Shen, “Leveraging radiation reaction via laser-driven plasma fields,” *Plasma Phys. Control. Fusion* **61**, 065007 (2019).
- <sup>32</sup>B. Martinez, E. d’Humières, and L. Gremillet, “Synchrotron emission from nanowire array targets irradiated by ultraintense laser pulses,” *New J. Phys.* **60**, 074009 (2018).
- <sup>33</sup>W. Luo, S.-D. Wu, W.-Y. Liu, Y.-Y. Ma, F.-Y. Li, T. Yuan, J.-Y. Yu, M. Chen, and Z.-M. Sheng, “Enhanced electron-positron pair production by two obliquely incident lasers interacting with a solid target,” *Plasma Phys. Control. Fusion* **60**, 095006 (2018).
- <sup>34</sup>L.-q. Zhang, S.-d. Wu, H.-r. Huang, H.-y. Lan, W.-y. Liu, Y.-c. Wu, Y. Yang, Z.-q. Zhao, Z.-c. Zhu, and W. Luo, “Brilliant attosecond  $\gamma$ -ray emission and high-yield positron production from intense laser-irradiated nano-micro array,” *Physics of Plasmas* **28**, 023110 (2021).
- <sup>35</sup>R. Capdessus, L. Gremillet, and P. McKenna, “High-density electron-ion bunch formation and multi-GeV positron production via radiative trapping in extreme-intensity laser-plasma interactions,” *Physics of Plasmas* **22**, 113003 (2020).
- <sup>36</sup>J. Y. Yu, T. Yuan, W. Y. Liu, M. Chen, W. Luo, S. M. Weng, and Z. M. Sheng, “QED effects induced harmonics generation in extreme intense laser foil interaction,” *Plasma Phys. Control. Fusion* **60**, 044011 (2018).
- <sup>37</sup>Z. Léczy and A. Andreev, “Minimum requirements for electron-positron pair creation in the interaction of ultra-short laser pulses with thin foils,” *Plasma Phys. Control. Fusion* **61**, 045005 (2019).
- <sup>38</sup>Y.-J. Gu, M. Jirka, O. Klimo, and S. Weber, “Gamma photons and electron-positron pairs from ultra-intense laser-matter interaction: A comparative study of proposed configurations,” *Matter and Radiation at Extremes* **4**, 064403 (2019).
- <sup>39</sup>J. Q. Yu, H. Y. Lu, T. Takahashi, R. H. Hu, Z. Gong, W. J. Ma, Y. S. Huang, C. E. Chen, and X. Q. Yan, “Creation of electron-positron pairs in photon-photon collisions driven by 10-pw laser pulses,” *Phys. Rev. Lett.* **122**, 014802 (2019).
- <sup>40</sup>J. F. Ong, T. Moritaka, and H. Takabe, “Optimizing the energies conversion in laser-electron beam collision,” *Physics of Plasmas* **26**, 033102 (2019).
- <sup>41</sup>T. G. Blackburn, “Radiation reaction in electron-beam interactions with high-intensity lasers,” *Reviews of Modern Plasma Physics* **4**, 5 (2020).
- <sup>42</sup>H.-Y. Zhang, L.-F. Gan, H.-B. Zhuo, B. Qiao, Y.-Y. Ma, and J.-Y. Dai, “Enhanced pair production in collisions of intense pulsed lasers with a high-energy electron beam,” *Phys. Rev. A* **100**, 022122 (2019).
- <sup>43</sup>M. Lobet, X. Davoine, E. d’Humières, and L. Gremillet, “Generation of high-energy electron-positron pairs in the collision of a laser-accelerated electron beam with a multipetawatt laser,” *Phys. Rev. Accel. Beams* **20**, 043401 (2017).
- <sup>44</sup>Z. Gong, R. H. Hu, J. Q. Yu, Y. R. Shou, A. V. Arefiev, and X. Q. Yan, “Radiation rebound and quantum splash in electron-laser collisions,” *Phys. Rev. Accel. Beams* **22**, 093401 (2019).
- <sup>45</sup>Y.-F. Li, Y.-Y. Chen, W.-M. Wang, and H.-S. Hu, “Production of highly polarized positron beams via helicity transfer from polarized electrons in a strong laser field,” *Phys. Rev. Lett.* **125**, 044802 (2020).
- <sup>46</sup>C. Slade-Lowther, D. D. Sorbo, and C. P. Ridgers, “Identifying the electron-positron cascade regimes in high-intensity laser-matter interactions,” *New J. Phys.* **21**, 013028 (2019).
- <sup>47</sup>Z. Gong, R. H. Hu, H. Y. Lu, J. Q. Yu, D. H. Wang, E. G. Fu, C. E. Chen, X. T. He, and X. Q. Yan, “Brilliant GeV gamma-ray flash from inverse Compton scattering in the QED regime,” *Plasma Phys. Control. Fusion* **60**, 044004 (2018).
- <sup>48</sup>A. R. Bell and J. G. Kirk, “Possibility of Prolific Pair Production with High-Power Lasers,” *Phys. Rev. Lett.* **101**, 200403 (2008).
- <sup>49</sup>A. M. Fedotov, N. B. Narozhny, G. Mourou, and G. Korn, “Limitations on the Attainable Intensity of High Power Lasers,” *Phys. Rev. Lett.* **105**, 080402 (2010).
- <sup>50</sup>S. S. Bulanov, T. Z. Esirkepov, A. G. R. Thomas, J. K. Koga, and S. V. Bulanov, “Schwinger Limit Attainability with Extreme Power Lasers,” *Phys. Rev. Lett.* **105**, 220407 (2010).
- <sup>51</sup>E. N. Nerush, I. Y. Kostyukov, A. M. Fedotov, N. B. Narozhny, N. V. Elkina, and H. Ruhl, “Laser Field Absorption in Self-Generated Electron-Positron Pair Plasma,” *Phys. Rev. Lett.* **106**, 035001 (2011).
- <sup>52</sup>N. V. Elkina, A. M. Fedotov, I. Y. Kostyukov, M. V. Legkov, S. B. Narozhny, E. N. Nerush, and H. Ruhl, “QED cascades induced by circularly polarized laser fields,” *Phys. Rev. Spec. Top. Accel. Beams* **14**, 054401 (2011).
- <sup>53</sup>M. Jirka, O. Klimo, S. V. Bulanov, T. Z. Esirkepov, E. Gelfer, S. S. Bulanov, S. Weber, and G. Korn, “Electron dynamics and  $\gamma$  and  $e^- e^+$  production by colliding laser pulses,” *Phys. Rev. E* **93**, 023207 (2016).
- <sup>54</sup>T. Grismayer, M. Vranic, J. L. Martins, R. A. Fonseca, and L. O. Silva, “Laser absorption via quantum electrodynamics cascades in counter-propagating laser pulses,” *Phys. Plasmas* **23**, 056706 (2016).
- <sup>55</sup>X.-L. Zhu, T.-P. Yu, Z.-M. Sheng, Y. Yin, I. C. E. Turcu, and A. Pukhov, “Dense GeV electron-positron pairs generated by lasers in near-critical-density plasmas,” *Nat. Commun.* **7**, 1 (2016).
- <sup>56</sup>M. Tamburini, A. D. Piazza, and C. H. Keitel, “Laser-pulse-shape control of seeded QED cascades,” *Sci. Rep.* **7**, 1 (2017).
- <sup>57</sup>A. Gonoskov, A. Bashinov, S. Bastrakov, E. Efimenko, A. Ilderton, A. Kim, M. Marklund, I. Meyerov, A. Muraviev, and A. Sergeev, “Ultrabright GeV Photon Source via Controlled Electromagnetic Cascades in Laser-Dipole Waves,” *Phys. Rev. X* **7**, 041003 (2017).
- <sup>58</sup>T. Grismayer, M. Vranic, J. L. Martins, R. A. Fonseca, and L. O. Silva, “Seeded QED cascades in counterpropagating laser pulses,” *Phys. Rev. E* **95**, 023210 (2017).
- <sup>59</sup>A. F. Savin, A. J. Ross, R. Aboushelbaya, M. W. Mayr, B. Spiers, R. H.-W. Wang, and P. A. Norreys, “Energy absorption in the laser-QED regime,” *Sci. Rep.* **9**, 1 (2019).
- <sup>60</sup>K. Qu, S. Meuren, and N. J. Fisch, “Signature of collective plasma effects in beam-driven QED cascades,” *Phys. Rev. Lett.* **127**, 095001 (2021).
- <sup>61</sup>Y. Shi, J. Xiao, H. Qin, and N. J. Fisch, “Simulations of relativistic quantum plasmas using real-time lattice scalar QED,” *Phys. Rev. E* **97**, 053206 (2018).
- <sup>62</sup>A. S. Samsonov, I. Y. Kostyukov, and E. N. Nerush, “Hydrodynamical model of QED cascade expansion in an extremely strong laser pulse,” *Matter and Radiation at Extremes* **6**, 034401 (2021), <https://doi.org/10.1063/5.0035347>.
- <sup>63</sup>J. Schwinger, “On gauge invariance and vacuum polarization,” *Phys. Rev.* **82**, 664 (1951).
- <sup>64</sup>A. Di Piazza, C. Müller, K. Z. Hatsagortsyan, and C. H. Keitel, “Extremely high-intensity laser interactions with fundamental quantum systems,” *Rev. Mod. Phys.* **84**, 1177 (2012).
- <sup>65</sup>I. V. Sokolov, N. M. Naumova, J. A. Nees, and G. A. Mourou, “Pair Creation in QED-Strong Pulsed Laser Fields Interacting with Electron Beams,” *Phys. Rev. Lett.* **105**, 195005 (2010).
- <sup>66</sup>H. Hu, C. Müller, and C. H. Keitel, “Complete QED Theory of Multiphoton Trident Pair Production in Strong Laser Fields,” *Phys. Rev. Lett.* **105**, 080401 (2010).
- <sup>67</sup>A. G. R. Thomas, C. P. Ridgers, S. S. Bulanov, B. J. Griffin, and S. P. D. Mangles, “Strong Radiation-Damping Effects in a Gamma-Ray Source Generated by the Interaction of a High-Intensity Laser with a Wakefield-Accelerated Electron Beam,” *Phys. Rev. X* **2**, 041004 (2012).
- <sup>68</sup>N. Neitz and A. Di Piazza, “Stochasticity Effects in Quantum

- Radiation Reaction,” *Phys. Rev. Lett.* **111**, 054802 (2013).
- <sup>69</sup>S. S. Bulanov, C. B. Schroeder, E. Esarey, and W. P. Leemans, “Electromagnetic cascade in high-energy electron, positron, and photon interactions with intense laser pulses,” *Phys. Rev. A* **87**, 062110 (2013).
- <sup>70</sup>T. G. Blackburn, C. P. Ridgers, J. G. Kirk, and A. R. Bell, “Quantum Radiation Reaction in Laser–Electron-Beam Collisions,” *Phys. Rev. Lett.* **112**, 015001 (2014).
- <sup>71</sup>D. G. Green and C. N. Harvey, “Transverse Spreading of Electrons in High-Intensity Laser Fields,” *Phys. Rev. Lett.* **112**, 164801 (2014).
- <sup>72</sup>M. Vranic, J. L. Martins, J. Vieira, R. A. Fonseca, and L. O. Silva, “All-Optical Radiation Reaction at  $10^{21}$  W/cm<sup>2</sup>,” *Phys. Rev. Lett.* **113**, 134801 (2014).
- <sup>73</sup>T. G. Blackburn, A. Ilderton, C. D. Murphy, and M. Marklund, “Scaling laws for positron production in laser–electron-beam collisions,” *Phys. Rev. A* **96**, 022128 (2017).
- <sup>74</sup>M. Vranic, O. Klimo, G. Korn, and S. Weber, “Multi-GeV electron-positron beam generation from laser-electron scattering,” *Sci. Rep.* **8**, 4702 (2018).
- <sup>75</sup>J. Magnusson, A. Gonoskov, M. Marklund, T. Z. Esirkepov, J. K. Koga, K. Kondo, M. Kando, S. V. Bulanov, G. Korn, and S. S. Bulanov, “Laser-particle collider for multi-gev photon production,” *Phys. Rev. Lett.* **122**, 254801 (2019).
- <sup>76</sup>C. Bula, K. T. McDonald, E. J. Prebys, C. Bamber, S. Boege, T. Kotseroglou, A. C. Melissinos, D. D. Meyerhofer, W. Ragg, D. L. Burke, R. C. Field, G. Horton-Smith, A. C. Odian, J. E. Spencer, D. Walz, *et al.*, “Observation of Nonlinear Effects in Compton Scattering,” *Phys. Rev. Lett.* **76**, 3116 (1996).
- <sup>77</sup>D. L. Burke, R. C. Field, G. Horton-Smith, J. E. Spencer, D. Walz, S. C. Berridge, W. M. Bugg, K. Shmakov, A. W. Weidemann, C. Bula, K. T. McDonald, E. J. Prebys, C. Bamber, S. J. Boege, T. Koffas, *et al.*, “Positron Production in Multiphoton Light-by-Light Scattering,” *Phys. Rev. Lett.* **79**, 1626 (1997).
- <sup>78</sup>G. White and V. Yakimenko, “On possible upgrades to FACET-II,” (2020), *personal communication*.
- <sup>79</sup>G. White and V. Yakimenko, “Ultra-short-z linear collider parameters,” (2018), [arXiv:1811.11782](https://arxiv.org/abs/1811.11782).
- <sup>80</sup>V. Yakimenko, S. Meuren, F. Del Gaudio, *et al.*, “Prospect of Studying Nonperturbative QED with Beam-Beam Collisions,” *Phys. Rev. Lett.* **122**, 190404 (2019).
- <sup>81</sup>E. Cartlidge, “The light fantastic,” *Science* **359**, 382 (2018).
- <sup>82</sup>J. Bromage, S.-W. Bahk, I. A. Begishev, C. Dorrer, M. J. Guardalben, B. N. Hoffman, J. Oliver, R. G. Roides, E. M. Schiesser, M. J. Shoup III, and *et al.*, “Technology development for ultraintense all-OPCPA systems,” *High Power Laser Sci* **7**, e4 (2019).
- <sup>83</sup>C. N. Danson, C. Haefner, J. Bromage, *et al.*, “Petawatt and exawatt class lasers worldwide,” *High Power Laser Sci. Eng.* **7**, e54 (2019).
- <sup>84</sup>C. N. Danson, C. Haefner, J. Bromage, T. Butcher, J.-C. F. Chanteloup, E. A. Chowdhury, A. Galvanauskas, L. A. Gizzi, J. Hein, D. I. Hillier, and *et al.*, “Petawatt and exawatt class lasers worldwide,” *High Power Laser Sci. Eng.* **7**, e54 (2019).
- <sup>85</sup>S. C. Wilks, J. M. Dawson, and W. B. Mori, “Frequency up-conversion of electromagnetic radiation with use of an overdense plasma,” *Phys. Rev. Lett.* **61**, 337 (1988).
- <sup>86</sup>E. Esarey, A. Ting, and P. Sprangle, “Frequency shifts induced in laser pulses by plasma waves,” *Phys. Rev. A* **42**, 3526 (1990).
- <sup>87</sup>W. M. Wood, C. W. Siders, and M. C. Downer, “Measurement of femtosecond ionization dynamics of atmospheric density gases by spectral blueshifting,” *Phys. Rev. Lett.* **67**, 3523 (1991).
- <sup>88</sup>K. Qu and N. J. Fisch, “Laser frequency upconversion in plasmas with finite ionization rates,” *Phys. Plasmas* **26**, 083105 (2019).
- <sup>89</sup>M. R. Shcherbakov, K. Werner, Z. Fan, N. Talisa, E. Chowdhury, and G. Shvets, “Photon acceleration and tunable broadband harmonics generation in nonlinear time-dependent metasurfaces,” *Nat. Commun.* **10**, 1345 (2019).
- <sup>90</sup>A. Nishida, N. Yugami, T. Higashiguchi, T. Otsuka, F. Suzuki, M. Nakata, Y. Sentoku, and R. Kodama, “Experimental observation of frequency up-conversion by flash ionization,” *Appl. Phys. Lett.* **101**, 161118 (2012).
- <sup>91</sup>K. Qu, Q. Jia, M. R. Edwards, and N. J. Fisch, “Theory of electromagnetic wave frequency upconversion in dynamic media,” *Phys. Rev. E* **98**, 023202 (2018).
- <sup>92</sup>M. R. Edwards, K. Qu, Q. Jia, J. M. Mikhailova, and N. J. Fisch, “Cascaded chirped photon acceleration for efficient frequency conversion,” *Phys. Plasmas* **25**, 053102 (2018).
- <sup>93</sup>S. S. Bulanov, A. M. Fedotov, and F. Pegoraro, “Damping of electromagnetic waves due to electron-positron pair production,” *Phys. Rev. E* **71**, 016404 (2005).
- <sup>94</sup>H. Peng, C. Riconda, S. Weber, C. T. Zhou, and S. C. Ruan, “Frequency conversion of lasers in a dynamic plasma grating,” *Phys. Rev. Applied* **15**, 054053 (2021).
- <sup>95</sup>R. G. Greaves and C. M. Surko, “An electron-positron beam-plasma experiment,” *Phys. Rev. Lett.* **75**, 3846 (1995).
- <sup>96</sup>B. D. Fried, “Mechanism for instability of transverse plasma waves,” *Phys. Fluids* **2**, 337 (1959).
- <sup>97</sup>M. R. Edwards, N. J. Fisch, and J. M. Mikhailova, “Strongly enhanced stimulated brillouin backscattering in an electron-positron plasma,” *Phys. Rev. Lett.* **116**, 015004 (2016).
- <sup>98</sup>V. B. Berestetskii, E. M. Lifshitz, and L. P. Pitaevskii, *Quantum Electrodynamics*, 2nd ed. (Butterworth-Heinemann, 1982).
- <sup>99</sup>M. Aicheler, P. Burrows, M. Draper, T. Garvey, P. Lebrun, K. Peach, N. Phinney, H. Schmickler, D. Schulte, and N. Toge, *A Multi-TeV Linear Collider Based on CLIC Technology: CLIC Conceptual Design Report*, CERN Yellow Reports: Monographs (CERN, Geneva, 2012).
- <sup>100</sup>A. Caldwell, K. Lotov, A. Pukhov, and F. Simon, “Proton-driven plasma-wakefield acceleration,” *Nature Phys.* **5**, 363 (2009).
- <sup>101</sup>T. D. Arber, K. Bennett, C. S. Brady, A. Lawrence-Douglas, M. G. Ramsay, N. J. Sircombe, P. Gillies, R. G. Evans, H. Schmitz, A. R. Bell, *et al.*, “Contemporary particle-in-cell approach to laser-plasma modelling,” *Plasma Phys. Contr. F.* **57**, 113001 (2015).
- <sup>102</sup>C. P. Ridgers, J. G. Kirk, R. Ducloux, T. G. Blackburn, C. S. Brady, K. Bennett, T. D. Arber, and A. R. Bell, “Modelling gamma-ray photon emission and pair production in high-intensity laser–matter interactions,” *J. Comput. Phys.* **260**, 273 (2014).
- <sup>103</sup>J.-X. Li, K. Z. Hatsagortsyan, B. J. Galow, and C. H. Keitel, “Attosecond Gamma-Ray Pulses via Nonlinear Compton Scattering in the Radiation-Dominated Regime,” *Phys. Rev. Lett.* **115**, 204801 (2015).
- <sup>104</sup>D. J. Kane and R. Trebino, “Characterization of arbitrary femtosecond pulses using frequency-resolved optical gating,” *IEEE J. Quantum Electron* **29**, 571 (1993).
- <sup>105</sup>C. Iaconis and I. A. Walmsley, “Spectral phase interferometry for direct electric-field reconstruction of ultrashort optical pulses,” *Opt. Lett.* **23**, 792 (1998).
- <sup>106</sup>A. J. Gonsalves, K. Nakamura, J. Daniels, *et al.*, “Petawatt laser guiding and electron beam acceleration to 8 gev in a laser-heated capillary discharge waveguide,” *Phys. Rev. Lett.* **122**, 084801 (2019).
- <sup>107</sup>V. Yakimenko, L. Alsberg, E. Bong, G. Bouchard, C. Clarke, C. Emma, S. Green, C. Hast, M. J. Hogan, J. Seabury, N. Lipkowitz, B. O’Shea, D. Storey, G. White, and G. Yocky, “FACET-II facility for advanced accelerator experimental tests,” *Phys. Rev. Accel. Beams* **22**, 101301 (2019).
- <sup>108</sup>S. Meuren, P. H. Bucksbaum, N. J. Fisch, F. Fiúza, S. Glenzer, M. J. Hogan, K. Qu, D. A. Reis, G. White, and V. Yakimenko, “On seminal hep research opportunities enabled by colocating multi-petawatt laser with high-density electron beams,” (2020), [arXiv:2002.10051](https://arxiv.org/abs/2002.10051) [physics.plasm-ph].
- <sup>109</sup>S. Meuren, D. A. Reis, R. Blandford, P. H. Bucksbaum, N. J. Fisch, F. Fiúza, E. Gerstmayr, S. Glenzer, M. J. Hogan, C. Pellegrini, M. E. Peskin, K. Qu, G. White, and V. Yakimenko,

“MP3 white paper 2021 – research opportunities enabled by co-locating multi-petawatt lasers with dense ultra-relativistic

electron beams,” (2021), [arXiv:2105.11607](https://arxiv.org/abs/2105.11607) [physics.plasm-ph].